J. Mech. Phys. Solids 149 (2021) 104341

Contents lists available at ScienceDirect

Journal of the Mechanics and Physics of Solids

journal homepage: www.elsevier.com/locate/jmps

Strong and Tough Bioinspired Additive-Manufactured Dual-Phase Mechanical Metamaterial Composites

Sha Yin[a,*], Weihua Guo[a], Huitian Wang[a,#], Yao Huang[a], Ruiheng Yang[a], Zihan Hu[a], Dianhao Chen[a], Jun Xu[b], Robert O. Ritchie[c,*]

[a] *Vehicle Energy & Safety Laboratory (VESL), Department of Automotive Engineering, School of Transportation Science & Engineering, Beihang University, Beijing 100191, China*

[b] *Vehicle Energy & Safety Laboratory (VESL), North Carolina Motorsports and Automotive Research Center, Department of Mechanical Engineering and Engineering Science, The University of North Carolina at Charlotte, Charlotte, NC 28223, USA*

[c] *Department of Materials Science & Engineering, University of California, Berkeley, CA 94720, USA*

ARTICLE INFO

Keywords:
Mechanical metamaterials
Composite lattice materials
Bioinspired design
Microstructural design
Energy absorption

ABSTRACT

Nature's materials are generally hybrid composites with superior mechanical properties achieved through delicate architectural designs. Inspired by the precipitation hardening mechanisms observed in biological materials as well as engineering alloys, we develop here dual-phase mechanical metamaterial composites by employing architected lattice materials as the constituent matrix and reinforcement phases. The composite metamaterials made from austenitic stainless steel are simply fabricated using selected laser melting based additive manufacturing. Using quasi-static compression tests and simulation studies, we find that strength and toughness can be simultaneously enhanced with the addition of reinforcement phase grains. Effects of reinforcement phase patterning and connectivity are examined. By fully utilizing the energy dissipation from phase-boundary slip, an optimized dual-phase metamaterial is designed with the maximum slip area, where every truss unit in the matrix phase is completely surrounded by reinforcement phase lattices; this material exhibits a specific energy absorption capability that is ~2.5 times that of the constituent matrix phase lattices. The design rationale for dissipative dual-phase metamaterials is analyzed and summarized with a focus on phase pattering. The present digital multiphase mechanical metamaterials can emulate almost any of nature's architectures and toughening mechanisms, offering a novel pathway to manipulate mechanical properties through arbitrary phase-material selection and patterning. We believe that this could markedly expand the design space for the development of future materials.

1. Introduction

Nature's materials are generally hybrid composites typically consisting of a hard mineral phase within a soft phase of organic molecules, which are structured into a highly sophisticated architecture over varying length-scales to create exceptional structural capabilities (Munch et al., 2008). As such, numerous designs and toughening motifs have been explored in biological materials

* Corresponding authors.
E-mail addresses: shayin@buaa.edu.cn (S. Yin), ritchie@berkeley.edu (R.O. Ritchie).
Current address: Changshu Automotive Trim Co., Ltd.

https://doi.org/10.1016/j.jmps.2021.104341
Received 25 September 2020; Received in revised form 30 November 2020; Accepted 25 January 2021
Available online 30 January 2021
0022-5096/

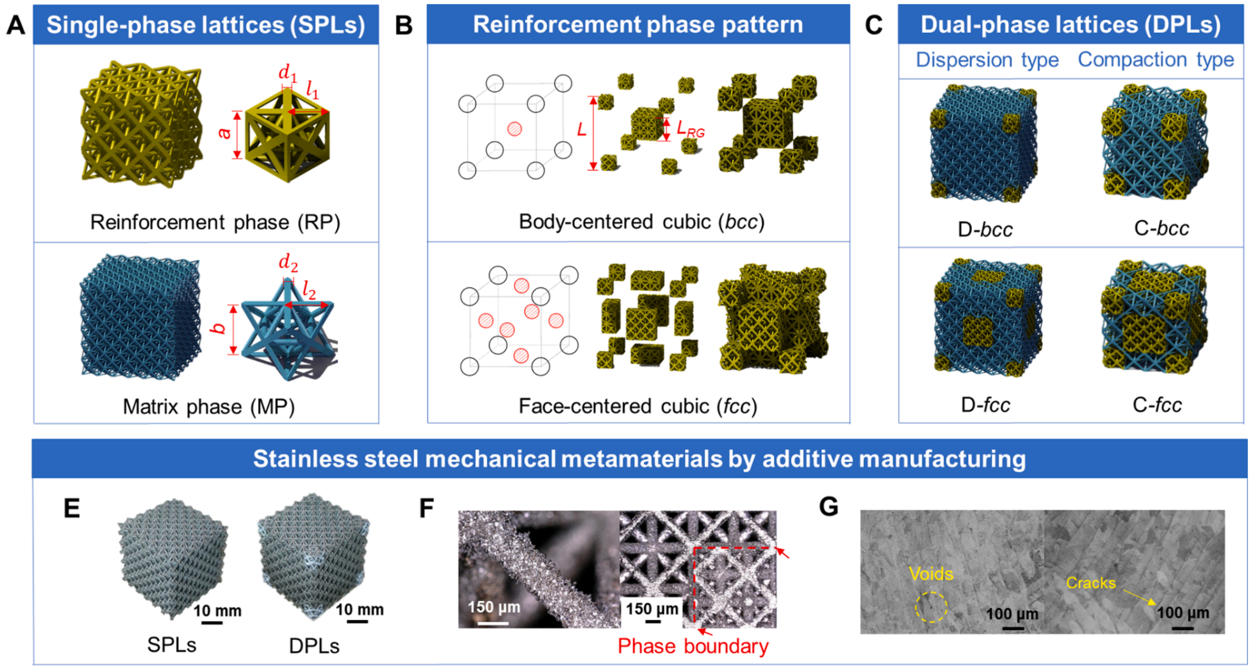

Fig. 1. Architecture design and fabrication of dual-phase lattices (DPLs). (A) Geometrical illustrations of two types of lattice materials, respectively as matrix phase (MP) and reinforcement phase (RP) of DPLs. (B-D) DPLs with *bcc* and *fcc* patterns of RP classified as dispersion type and compaction type according to interactions between the reinforcement grains. (E) DPL samples fabricated by selected laser melting based additive manufacturing together with the single-phase counterparts. (F) Mesoscopic printing details. (G) Manufacturing defects observed.

(Velasco-Hogan et al., 2018); for example, the stomatopod dactyl club of "smasher-type" mantis shrimp features a Bouligand-type (twisted plywood) structure (Weaver, 2012), with newly identified randomly distributed voids between the chitin fibers and protein matrix (Yin et al., 2020), which creates a hard yet high toughness material. Nacre and conch shells are also well known for their complex "brick-and-mortar" architectures, which generate toughness properties that far exceed what could be expected from a simple mixture of their components (Gu et al., 2017; Aizenberg, 2005). Similarly, pomelo peel, which provides a natural protecting barrier for pulp and seed, possesses excellent energy dissipation capability due to the arrangement of vascular bundles which serve as local reinforcements (Thielen et al., 2013; Zhang et al., 2019a), akin to the precipitation hardening mechanisms observed in metallic alloys (Jin et al., 2018). Additionally, co-continuous systems exist in Nature comprising a biological design of two interpenetrating materials - one soft, the other hard - which can provide outstanding energy dissipation due to mutual constraint between the two phases (Wang et al., 2011; Lee et al., 2012; Liu and Wang, 2015).

One way to mimic such biological materials is through the concept of lattice materials. These are ordered architected materials which have attracted wide attention over the past decade as synthetic mechanical metamaterials with mechanical properties tailored by microstructure (Evans, 2001). For example, Deshpande et al. (2001a, 2001b) investigated the topological criteria that dictate the stretching- or bending-dominated deformation of pin-jointed truss frameworks, a study that indicated that stretching-dominated lattice materials should satisfy Maxwell's criterion for static determinacy and be more weight-efficient than bending-dominated foams in structural applications. With various developed fabrication methodologies, lattice materials can be produced from metals (Wadley, 2006), polymers (Yin et al., 2013), fiber composites (Wang et al., 2010) and ceramics (Meza and Greer, 2014), but their microstructure design is still severely limited by fabrication. A case in point are Kagome and pyramidal lattice topologies with hollow trusses (Evans et al., 2010; Pingle et al., 2010), where their complicated geometries are still not feasible to fabricate in practice.

However, with the rapid development of 3D printing, various complex architectures in these materials are now feasible to fabricate by new additive manufacturing methods and examine in terms of novel unit designs and new deformation mechanisms. Recent advances regarding novel unit designs have involved the development of a new type of ultralow density material, termed "Shellular", with a continuous shell structure, which is anticipated to overcome the geometrical incompleteness often found in previous lattice materials with hollow trusses (Han et al., 2015). Additionally, the study of Berger et al. (2017) identified a material geometry that can achieve the Hashin-Shtrikman upper bounds on isotropic elastic stiffness with a stiff but well distributed network of plates. It is apparent that as metamaterials, 3D plate-lattices can exhibit optimal isotropic stiffness together with isotropic yield strength (Tancogne-Dejean et al., 2018). With a focus on dissipative lattices, recently a bi-material concept comprising stretch-dominated lattices at one end and tensegrities of tensile and compressive struts at the other, has been proposed by Ruschel and Zok (2020). Indeed, robust and damage-tolerant crystal-inspired architected materials have been developed using the same hardening mechanisms found in crystalline materials, such as grain-boundary hardening, precipitation hardening (Gazizov and Kaibyshev, 2017; Jin et al., 2018; Yashpal et al., 2017) and multi-phase hardening (Wu et al., 2017), to create desired properties (Pham et al., 2019). Other self-similar

Table 1
Geometry parameters for the dual-phase lattices (DPLs) and their constituent single-phase lattices (SPLs).

Lattice type	d_1 (mm)	d_1/l_1	d_2 (mm)	d_2/l_2	L (mm)	Reinforcement grain unit number	$\overline{V}_{RP}$	$\overline{\rho}$	
								Theoretical	Experimental
MP	/	/	0.6	0.14	/	/	/	0.11	0.16
RP	0.6	0.21	/	/	/	/	/	0.27	0.38
D-*bcc*	0.6	0.21	0.6	0.14	36	$3 \times 3 \times 3$	0.07	0.12	0.18
D-*fcc*					36	$3 \times 3 \times 3$	0.15	0.12	0.20
C-*bcc*					24	$3 \times 3 \times 3$	0.25	0.13	0.24
C-*fcc*					24	$3 \times 3 \times 3$	0.50	0.14	0.28

Note: d represents the lattice truss diameter and l the length of the phase with the subscript 1 referring to the reinforcement phase and 2 to the matrix phase;
$\overline{V}_{RP}$ is the volume fraction of reinforcement phase grains in the DPLs; $\overline{\rho}$ is the relative density of DPLs, which is defined as the ratio of the volume of solid trusses to the overall volume.

hierarchical lattice materials have been designed with disparate features spanning multiple length-scales from nanometers to millimeters using various 3D printing technologies (Meza et al., 2014, 2015; Wu et al., 2019; Yin et al., 2018; Zheng et al., 2016). Referring to new deformation mechanisms, a class of multi-stable architected materials has been designed to exhibit controlled trapping of elastic energy, which provides a novel snap-through strategy to enhance energy absorption (Shan et al., 2015); these materials can also be made to achieve a shape-reconfigurable function (Haghpanah et al., 2016). Zhang et al. (2019b) has developed the theoretical framework for programming static periodic topological solitons into metamaterials based on multi-stable systems. However, most of the above proposed structural designs for mechanical lattice materials have to date been based on single-phase materials, where the design space is still limited.

The objective of the current work is to introduce the existing toughening mechanisms in biological or metallic materials into the design of mechanical metamaterials, and develop multi-phase strong and tough metamaterial composites where the design space will be markedly expanded as each phase and phase arrangement can be manipulated to form digital composites with tailorable phase patterns. Here, specifically, dual-phase lattices with programmed patterns of the reinforcement phase are designed and fabricated simply using single-material additive manufacturing, with experimental and simulation studies carried out to explore their stiffness and strength, toughness and energy absorption capabilities. In addition, the effects of geometry and patterning of the reinforcement phase are examined in order to generate guidelines for the design of stronger and tougher digital metamaterials with excellent energy absorption properties.

2. Materials and methods

2.1. Design

Akin to the precipitation hardening mechanism in metals, dual-phase lattices (DPLs) were designed as novel mechanical metamaterials consisting of architected truss materials (single-phase lattices, SPLs) with a matrix phase (MP) and reinforcement phase (RP), as illustrated in Figure 1A. The mechanical properties of the matrix phase and reinforcement phase SPLs were different and were manipulated in this study by varying their microstructures. We selected face-centered cubic (*fcc*) lattice materials for the matrix phase, and simple cubic and face-centered cubic (*sc-fcc*) lattice materials (Mohr, 2018) for the reinforcement. The reinforcement phase grains were patterned into *bcc* (body-centered cubic) and *fcc* forms, and incorporated into matrix phase lattice materials, as shown in Figure 1B-C after cautious design at the phase boundaries to guarantee complete connection between the trusses. Depending on the spatial distribution distance among reinforcement phase grains, these dual-phase lattices can be classified as dispersion type (D-*bcc* and D-*fcc*) DPLs as $L > 2L_{RG}$ (Fig. 1C), and compaction type (C-*bcc* and C-*fcc*) DPLs as $L = 2L_{RG}$ (Fig. 1D) when the reinforcement grains are in contact, where L is the distance in the compression direction between each two reinforcement grains, and L_{RG} is the side length of reinforcement grain.

The relative density of SPLs in the present study was derived, respectively, as $\overline{\rho}_{RP} = \frac{3+12\sqrt{2}\pi}{8}\left(\frac{d_1}{l_1}\right)^2$ and $\overline{\rho}_{MP} = \frac{3\sqrt{2}\pi}{2}\left(\frac{d_2}{l_2}\right)^2$, where $d_1 = 0.6mm$, $l_1 = 2.8mm$ and $d_2 = 0.6mm$, $l_2 = 4.2mm$; here d represents the lattice truss diameter and l the length of the phase with the subscript 1 referring to the reinforcement phase and 2 to the matrix phase. However, for those with higher relative densities (> 0.1), the coincident volume at the joints of the lattice members must be considered (Yin et al., 2018). A curve fit of the relative densities calculated by computer-aided design models of these two SPLs suggested adding a cubic correction, given as:

$$\overline{\rho}_{RP} = \frac{3+12\sqrt{2}\pi}{8}\left(\frac{d_1}{l_1}\right)^2 - 8.4496\left(\frac{d_1}{l_1}\right)^3 \quad (1)$$

$$\overline{\rho}_{MP} = \frac{3\sqrt{2}\pi}{2}\left(\frac{d_2}{l_2}\right)^2 - 6.8282\left(\frac{d_2}{l_2}\right)^3 \quad (2)$$

For DPLs, the relative density, determined by the proportion and the relative densities of each single phase, can be expressed as:

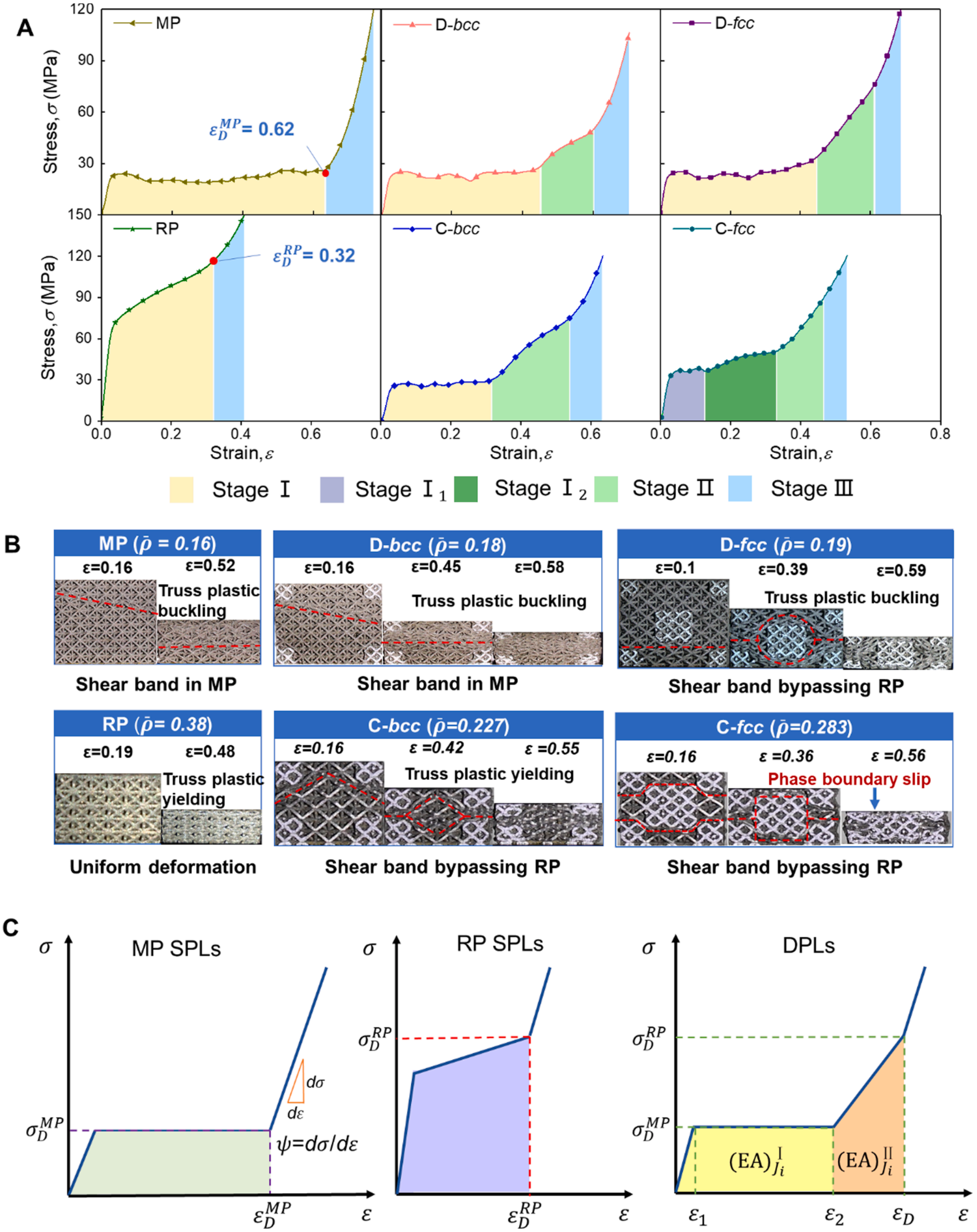

Fig. 2. Compressive response of various types of DPLs as compared to constituent SPLs. (A) Compressive stress-strain curves. (B) Typical deformation and failure modes illustrating localized shear bonds in the different materials. (C) The idealized compressive responses of the matrix phase, reinforcement phase SPLs and DPLs.

$$\overline{\rho} = \overline{\rho}_{RP}\overline{V}_{RP} + \overline{\rho}_{MP}\overline{V}_{MP} \tag{3}$$

with $\overline{V}_{RP} = V_{RP}/V \text{and} \overline{V}_{MP} = V_{MP}/V$ as the respective volume fractions of the reinforcement phase and matrix phase, where $\overline{V}_{RP}$, $\overline{V}_{MP}$ are the volumes of the RP and MP respectively in the DPLs. The overall volume of the DPLs is designated as V. All geometrical parameters are summarized in Table 1.

2.2. Fabrication

The dual-phase mechanical metamaterials were fabricated by additive manufacturing using stainless steel powders, together with constituent single-phase truss lattice materials. Selective laser melting (SLM) based additive manufacturing was employed for the fabrication of all the dual-phase metamaterials on an EOS M280 printer using stainless steel powder. The advantages of SLM included the production of flexibly customized, complex parts with a high resolution of 40 μm and remarkable mechanical properties. Before the heating process, a layer of AISI 316 L austenitic stainless steel powder was spread on the surface of a build platen. A galvanometer was utilized to direct a laser beam across this surface to melt powder where necessary, fusing it with the layer below. Then the platen was lowered followed by the same fusing process, repeated until finishing. The fabricated DPLs samples are shown in Fig. 1E with the mesoscale details of the struts and phase boundaries illustrated in Fig. 1F. The evenly spaced parallel stripes that appear in metallographic images are related to the manufacturing method by melting stainless steel powders layer by layer. Manufacturing defects, such as interval between layers, air holes and cracks, were observed (Fig. 1G), and are attributed to the imperfect manufacturing process, *e.g.*, overly fast melting or too fast a condensation speed, inadequate power which can trigger incomplete powder melting and weak interlaminar bonding. The predicted relative densities of these lattice materials were calculated as shown in Table 1, and found to be ~30% to 48% smaller than our experimental values. Two main reasons exist for these discrepancies: one associated with the printing parameters, especially the laser spot compensation; the other one associated with the nature of the scraper during printing. Thus, further optimization of the printing process is warranted.

2.3. Mechanical testing

Quasi-static compression tests for the dual-phase lattice materials were carried out and their compressive behavior analyzed and compared with those of the single-phase counterparts. All the specimens were compressed on a universal electromechanical testing machine (MTS Exceed E64, MTS Systems China, Shenzhen) at a constant cross-head strain rate of $\sim 10^{-3}$/s. At least three tests were carried out for each group of specimens to ensure repeatability. The morphologies and failure modes after the compression tests for all the samples were observed in a KEYENCE VHX-6000 optical microscope (Keyence, Osaka, Japan). Videos were also recorded during the compression testing for further analysis (Canon EOS 80D).

3. Results and discussion

3.1. Mechanical Properties

3.1.1. Compressive response

The compressive (engineering) stress-strain curves of all the specimens together with their corresponding deformation history are shown in Figs. 2A-B. For D-*bcc* and D-*fcc* type DPLs, the compressive response typically included three stages: MP dominated deformation (Stage I), RP dominated deformation (Stage II) and densification (Stage III). In Stage I, the stress initially increased linearly until reaching a peak followed by a long stress plateau stage; the plateau region was characterized by small stress fluctuations which accompanied localized plastic buckling in the trusses that formed macroscopic shear bands in the matrix phase (indicated by the red line in Fig. 2B). In Stage II, with the densification of matrix phase, the stiffer reinforcement phase started to markedly deform; this induced a stress increase prior to final densification of the DPLs in Stage III. This behavior had been widely observed for other compaction type DPLs, as shown in Fig. 2A. However, as the reinforcement grains were connected to each other in the C-*bcc* and C-*fcc* type DPLs, the surrounding interconnected reinforcement grains in these materials tended to deform with the matrix phase. Additionally, in Stage I, phase-boundary slip accompanied by truss twist and fracture around the phase boundaries was observed and clearly contributed to strain hardening; this was especially evident in Stage I_2 for the C-*fcc* type DPLs. The governing failure mode of the DPLs was generally plastic buckling of the lattice trusses in the matrix phase. Shear localization bands originated in these matrix phase lattice units at regions of stress concentration close to the reinforcement grains. These bands then propagated by bypassing the reinforcement grains, as shown in Fig. 2B; the appearance of the shear bands thus depended on the patterns of the reinforcement phase.

In contrast, for the constituent single-phase lattices (SPLs), the representative stress-strain curves were similar to those observed in the DPLs but without the interacted deformation from the second phase. A long stress plateau stage was apparent for matrix phase SPLs, whereas a marked strain-hardening period was seen for the reinforcement phase SPLs following the initial linear-elastic stage (Fig. 2A). Matrix phase SPLs failed initially by the plastic buckling of limited lattice cells, which then created a shear localization band followed by progressive crushing layer by layer; however, reinforcement phase SPLs with ~2.4 times higher relative density tended to deform uniformly and failed by plastic yielding without the appearance of shear bands. The idealized compressive responses of the matrix phase, reinforcement phase SPLs and DPLs were quite distinct and are illustrated in Fig. 2C; the definition of all the critical points is elucidated in Appendix B. Note that the densification strain of the reinforcement phase SPLs, which failed by plastic yielding,

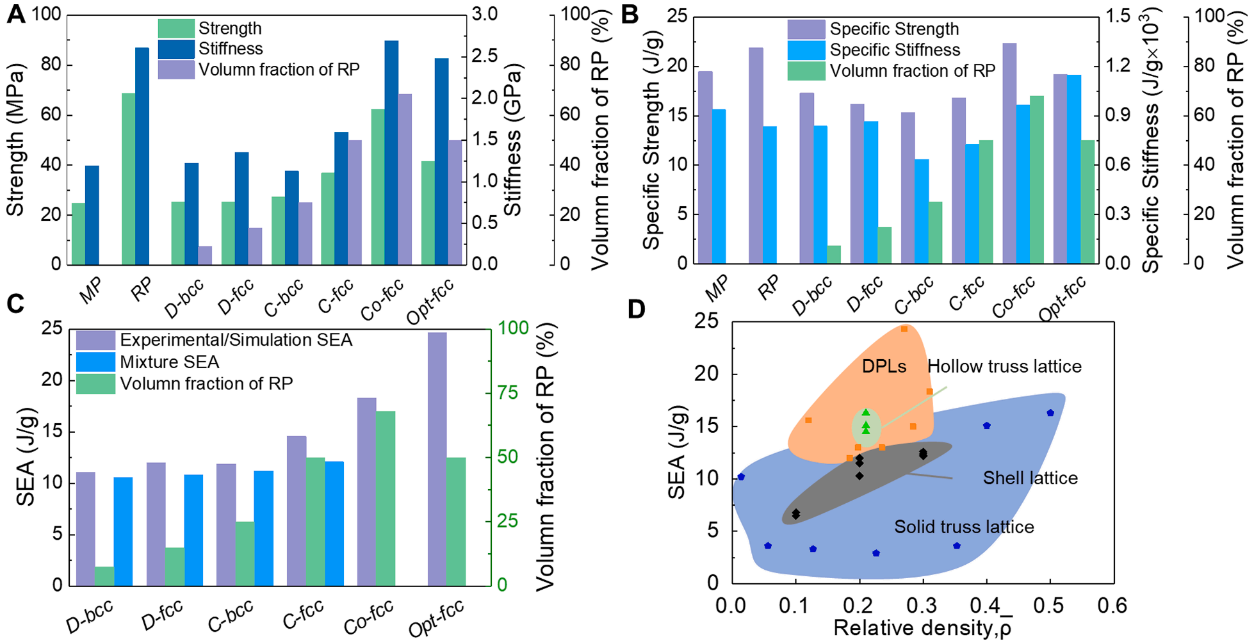

Fig. 3. Mechanical properties of DPLs. (A) Stiffness and strength. (B) Specific stiffness and strength compared to constituent SPLs. (C) Specific energy absorption (SEA) of DPLs with different volume fractions of RP, compared to results computed from the simple law of mixtures. (D) SEA of DPLs as a function of relative density for existing lattice materials fabricated similarly by additive manufacturing, showing that the dual-phase lattices developed in the present study show outstanding promise as tough, yet lightweight, materials.

is smaller than that of the matrix phase SPLs, which failed by plastic buckling; however, the densification stress of the reinforcement phase SPLs is larger.

3.1.2. *Compressive stiffness and strength*

The experimentally measured compressive stiffness and strength values, together with the corresponding specific stiffness and strength values, for the DPLs are shown in Figs. 3A-B. With regards to compressive stiffness, the experimental values of the D-*bcc*, D-*fcc*, C-*bcc*, and C-*fcc* type DPLs shown in Fig. 3A were, respectively, ~15%, 27%, 7.5% and 50% larger than those of the matrix phase SPLs. Indeed, the compressive stiffness of the DPLs was governed by both the volume fraction and pattern of the reinforcement grains; this is theoretically validated in Appendix A by assuming negligible interactions within each column. The compressive strength of the D-*bcc* and D-*fcc* type DPLs, with reinforcement phase volume fractions of, respectively, $\overline{V}_{RP}$= 7.4% and 14.8%, were almost the same as those of the constituent MP SPLs. We can conclude from this that the volume fraction of reinforcement grains does not correlate directly with the compressive strength (Fig. 3A) for discrete type DPLs. However, the strength values of the C-*bcc* type DPLs with a $\overline{V}_{RP}$of 25% were ~10% higher, while those of C-*fcc* type DPLs with a larger $\overline{V}_{RP}$ of 50% were significantly increased by ~49%, as compared with corresponding values for the constituent materials without the addition of reinforcement phases. Accordingly, in addition to the volume fraction, the connections between the reinforcement grains clearly play an important role in determining the compressive strength. The C-*fcc* type DPLs had 32 connection nodes while the C-*bcc* type DPLs only had 8. With the reinforcement grains strongly connected, this creates a co-continuous system that can deform in unison; this is the primary role of the reinforcement grains and their specific contribution to compressive strength. Accordingly, in this respect, the C-*fcc* type DPLs demonstrated the best performance. For dispersion type DPLs, the matrix phase dominated the deformation as in the initial stages, with the separated reinforcement phases acting like inclusions surrounded by a matrix phase; as they rarely deformed, they naturally contributed little to the compressive strength. Additionally, the specific stiffness and strength values (stiffness and strength per unit mass) of the DPLs were also analyzed and compared; these specific values were generally less than those of the constituent SPLs (Fig. 3B).

3.1.3. *Energy absorption*

Energy absorption can generally be regarded as an index to estimate the toughness of materials; it can be simply estimated from the area under the load-displacement curve up to the densification strain ε_D , as illustrated by the idealized compressive stress-strain curves in Fig. 2C. For dual-phase lattice materials, on account of two compression stages before densification, the traditional approach of determining the energy-absorption efficiency to calculate the densification strain is not suitable (Deng et al., 2019). Based on the corresponding compression characteristics, a criterion for the densification strain of the DPLs, ε_D, is defined here when the reinforcement phase is fully densified and reaches its densification stress, σ_D^{RP}, as tested separately for the reinforcement phase SPLs and

Table 2
Mechanical properties of all DPLs as compared with those of their constituent SPLs.

Materials	Stiffness (MPa) Theoretical	Experimental	Strength (MPa)	Energy absorption (J)	Specific stiffness (J/g)	Specific strength (J/g)	SEA (J/g)
MP SPL	1182	1063.7	24.8	654	937.4	19.5	9.7
RP SPL	2881	2605.0	68.6	601	835.9	21.9	13.9
D-*bcc* PL	1246	1223.0	25.2	788	837.1	17.3	11.1
D-*fcc* DPL	1311	1351.1	25.2	917	865.9	16.2	12.0
C-*bcc* DPL	1429	1143.2	27.2	305	636.7	15.3	11.9
C-*fcc* DPL	1676	1595.3	36.9	454	726.8	16.8	14.2
Co-*fcc* DPL	/	2692.6	62.4	675	964.4	22.4	18.3
Opt-*fcc* DPL	/	2480.2	41.6	724	1148.6	19.3	24.3

shown in Fig. 2A. For a column consisting of the largest reinforcement grain number in the DPLs, assuming that the stress remains constant through the thickness during compression and neglecting the interactions from other columns, the contribution to the densification strain, ε_D, from both the densified matrix and reinforcement phases can be expressed by:

$$\varepsilon_D = \frac{n-k}{n}\left(\varepsilon_D^{MP} + \Delta\varepsilon\right) + \frac{k}{n}\varepsilon_D^{RP} \tag{4}$$

where n is the overall cell number and k is the cell number of the reinforcement grains in this column, $\Delta\varepsilon = (\sigma_D^{RP} - \sigma_D^{MP})/\psi$ represents the extra deformable strain after matrix phase densification when the stress reaches the densification stress of the reinforcement phase σ_D^{RP} (ψ is the densification index that can be obtained from the compressive curves of the matrix phase SPLs in Fig. 2A); $\varepsilon_D^{MP}$and ε_D^{RP} are, respectively, the densification strain of the matrix and reinforcement phase SPLs. From the perspective of attaining a large macroscopic strain, with $\varepsilon_D^{RP} < \varepsilon_D^{MP}$, the selection of SPLs with a buckling-dominated failure mode will contribute to a greater densification strain of the DPLs. However, if the densification stress of the matrix and reinforcement phases differs significantly, the further deformable strain of the matrix phase SPLs will additionally contribute to the densification strain ε_D and energy absorption.

The energy absorption per unit volume, which is theoretically derived in Appendix B, indicates that the densification strain and stress of each phase, and the difference between the densification stress of the two phases, should be as high as possible for greater energy absorption. The specific energy absorption (SEA), *i.e.*, energy absorption per unit mass, was calculated from the experimental compressive curves as shown in Fig. 3C. With the addition of reinforcement grains, SEA values for the DPLs were always larger than those for the constituent SPLs. C-*fcc* type DPLs displayed the highest specific energy adsorption values, which were ~55% higher than those for the matrix phase SPLs and even ~5% higher than those of the reinforcement phase SPLs. However, theoretical SEA values using the rule of mixtures were also calculated and found to be lower than the experimental values. This was ascribed to the specific interactions between the two phases, including the sliding displacements between the phases which clearly contribute to the overall energy absorption; we further examine this as a toughening mechanism below. SEA values are plotted as a function of the relative density for our DPLs in Fig. 3D and are compared with values reported in the literature for other lattice materials; these include metallic single-phase lattices (Velasco-Hogan et al., 2018; Wu et al., 2019), shell lattices (Mohr, 2017) and hollow lattices (Evans et al., 2010; Pingle et al., 2010). These results indicate that the dual-phase lattices developed in the present study show outstanding promise as tough, yet lightweight, materials. Their mechanical properties are summarized in Table 2.

3.2. Numerical simulation

Finite element analysis (FEA) was performed to investigate the effects of geometry parameters on the compressive properties and toughness of the dual-phase lattice materials using an explicit dynamics finite element analysis approach (LS-DYNA, Livermore, USA). The dual-phase lattice materials were built up with trusses of measured diameter, and compressed between two stiff plates both meshed with solid elements. To select the appropriate element size, a mesh convergence analysis was performed and an element size of 1.0 mm was selected to ensure accurate results with a high calculation efficiency. The material properties were measured and set to be ideally elastoplastic in the simulation model, with a Young's modulus of 38 GPa, Poisson's ratio of 0.3, yield strength of 460 MPa and plastic region model with plastic failure strain of 0.5. In this model, two types of contacts were employed. An automatic general contact was adopted to simulate the contact among lattice trusses, whereas an automatic node-to-surface contact was chosen between lattice trusses and compression plates. To improve the calculation efficiency, an implicit-explicit switch simulation method was utilized here, where the implicit method improved the accuracy of calculation whereas the explicit method ensured the convergence of calculation (Yin et al., 2018).

To validate this compression model, the simulated stress-strain curves and deformation modes were compared with experimental results for all four types of DPLs; the comparison is shown in Fig. 4. The simulated stress-strain curves before densification exhibited characteristics with two stress plateaus, while the simulated strength values matched well with the experimentally measured values. Furthermore, the distribution of shear bands in the simulation results was almost the same as that observed experimentally for the DPLs. The results indicated that although nanoscale defects during additive manufacturing undoubtedly existed and can be challenging to control, their effect on the mechanical properties was not large after employing the measured truss geometry and mechanical properties. The compressive response of the constituent SPLs was also simulated. For the matrix phase SPLs, the simulation stress-strain

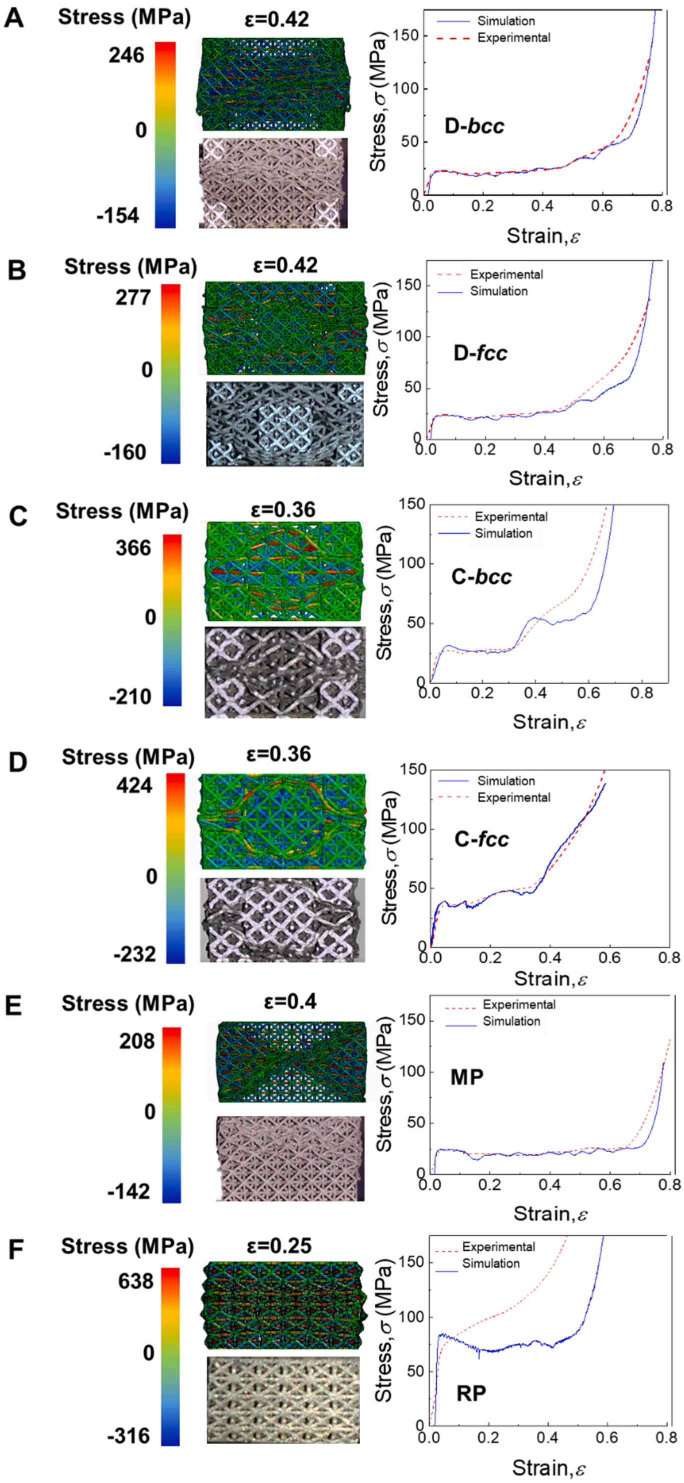

Fig. 4. Compression models for various types of mechanical metamaterials validated by experimental results. (A) D-*bcc* type DPLs. (B) D-*bcc* type DPLs. (C) C-*fcc* type DPLs. (D) C-*fcc* type DPLs. (E) Matrix phase SPLs. (F) Reinforcement phase SPLs.

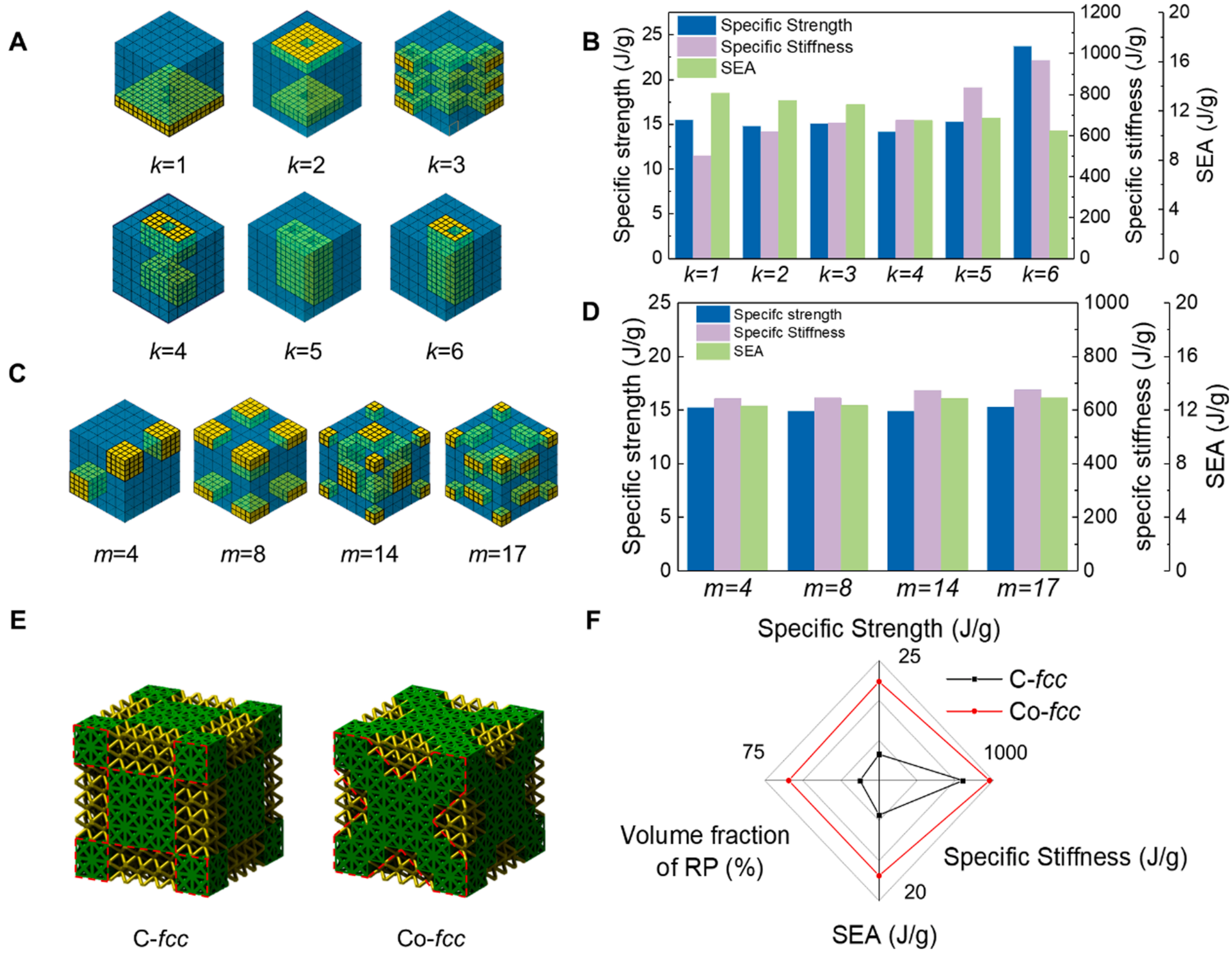

Fig. 5. Effects of reinforcement grains on mechanical properties of DPLs. (A-B) Stiffness, strength and energy absorption of DPLs with various reinforcement grain numbers in each column *k*. (C-D) Stiffness, strength and energy absorption of DPLs with increasing complexity and reinforcement grain numbers *m* at constant volume fraction $\overline{V}_{RP}$. (E-F) Co-continuous DPLs with overlapped RGs (termed as Co-*fcc* type), as compared with C-*fcc* type DPL

curves agreed well with the experimental results (Fig. 4E); however, differences were evident between the experimental and simulation stress-strain curve results for the reinforcement phase SPLs (Fig. 4F). We believe that this indicated that the nodal volume effects could not be neglected for lattice materials with a higher relative density during compression modeling.

3.3. Effects of reinforcement grain patterns

The volume fraction of the reinforcement phase can naturally affect the stiffness, strength and energy absorption of DPLs, as discussed above. However, as the arrangement of the reinforcement grains will determine the interactions between the matrix phase and reinforcement phase lattices, this was also explored to discern whether such effects could further enhance mechanical properties to guide the optimal design of these materials. Numerical simulations were performed for DPLs with various complexity of the reinforcement grains.

For the same volume fraction of reinforcement grains, DPLs with various numbers of reinforcement grains *k* in each column were examined in Fig. 5A-B. The simulation results revealed that the stiffness varied linearly with *k*. However, the strength values only increased if the reinforcement grains occupied all of the columns, *i.e.*, $k = 6$; otherwise, the MP lattice cells controlled the mode of deformation and the failure mechanism. The densification strain of the DPLs, shown in Eq. 4, was determined by the column with the largest reinforcement grain number *k*; as this tended to decrease with *k*, the specific energy absorption capacity was also decreased.

In addition, DPL models were developed for different dispersions of reinforcement grains by changing the reinforcement grain size to give various overall grain numbers *m* in the DPLs but at a constant overall volume fraction of reinforcement phase $\overline{V}_{RP}$ (Fig. 5C). Although shear banding in the matrix material was quite different including their initial position and propagation path (Fig. 6), the stiffness, strength, and specific energy absorption values were all found to increase slightly with *m* (Fig. 5D). This was attributed to the

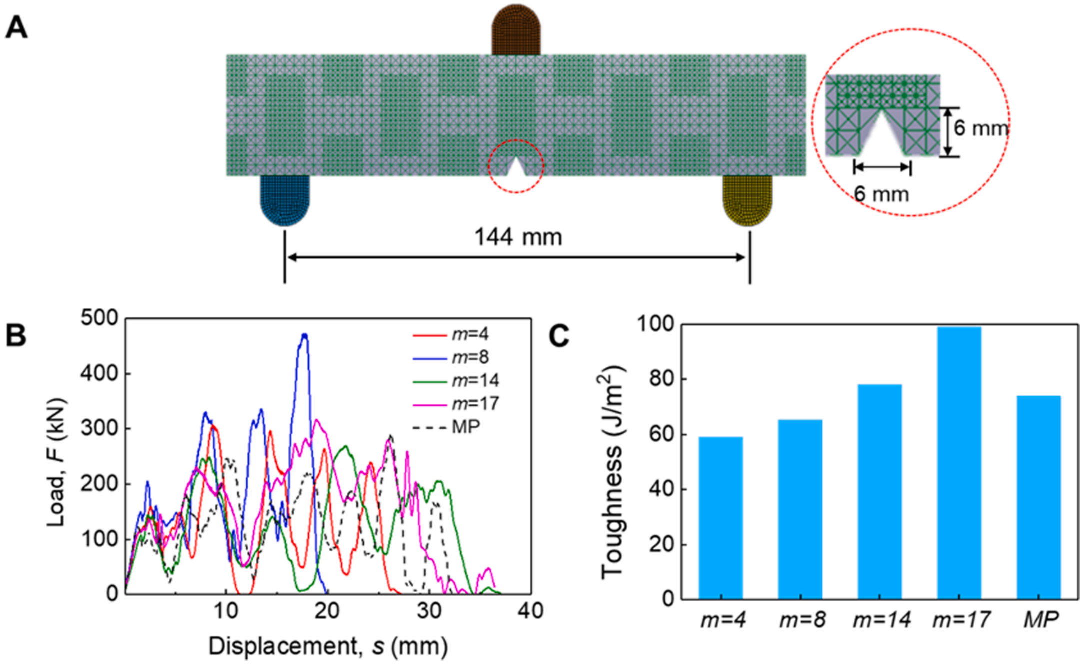

Fig. 6. Toughness simulation models of DPLs. (A) Cracked DPLs in three-point bending. (B) Simulation results. (C) Toughness comparison for DPLs with different RP distribution complexity.

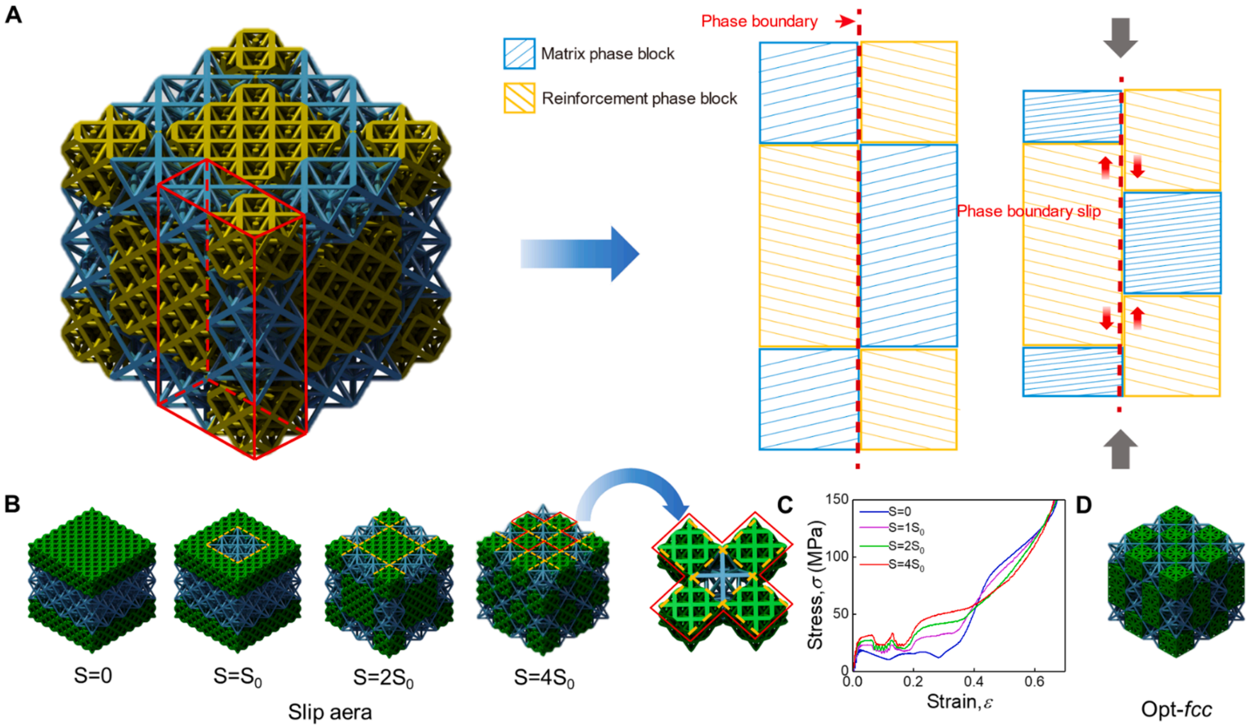

Fig. 7. Effects of phase-boundary slip on mechanical properties of DPLs. (A) Illustration of phase boundary accompanying RGs sliding for C-*fcc* type DPLs. (B-C) DPLs with various phase-boundary slip areas and their compressive performance. (D) Optimized DPLs with the maximum slip area, named as Opt-*fcc*.

failure being controlled by the matrix phase with the lack of any interaction of the shear bands with the reinforcement phase.

Additionally, our simulations addressed the question of the fracture toughness of our dual-phase mechanical metamaterials after incorporation of the reinforcement phase. Cracked models with different reinforcement grain numbers m under three-point bending were simulated and compared with the constituent matrix phase SPLs, as shown in Fig. 6. During crack propagation, if the crack tip encountered a high-energy phase (reinforcement grain), the crack became locally arrested and deflected into matrix phase or the phase boundaries. Accordingly, the work of fracture increased, compared to that of the SPLs, if the reinforcement grains were located along the crack propagation direction, specifically in this study for $m = 14$ and 17. The consequence of this is that the toughness increased with overall reinforcement grain number m.

3.4. Effects of reinforcement grain connectivity

The dispersion and compaction type of the DPLs, *e.g.*, D-*bcc* type and C-*bcc* type, performed differently from our experimental results (Fig. 2) because the incorporated reinforcement grains, when discretely distributed, had little effect on the stiffness and strength. Accordingly, the effects of the connectivity of the reinforcement grains were further examined by simulation. DPLs with overlapped reinforcement grains were designed forming co-continuous DPLs (termed as Co-*fcc* DPLs), as shown in Fig. 5E, and then (virtually) compressed. By comparing with the corresponding C-*fcc* type DPLs, results in Fig. 5F reveal that the specific stiffness, specific strength and specific energy absorption of the Co-*fcc* DPLs with a $\overline{V}_{RP}$ of 68% increased by 33%, 33% and 26%, respectively. This specific strength is almost 4 times of that of the matrix phase SPLs, and even surpassed that of constituent reinforcement phase lattice materials. In addition to the energy absorption resulting from the stronger RP scaffold, the trapped MP was constrained to deform with the RP which generated additional energy absorption. Accordingly, the increased connectivity of the reinforcement grains, together with a compatible geometry between two structured phases where all trusses are connected, served to enhance the overall mechanical properties by generating more deformation and plastic energy absorption. However, the RP scaffold in the co-continuous DPLs exhibited different reinforcement grain numbers k in each column, which resulted in non-uniform deformation such that all the lattice units were not fully deformed.

3.5. Effects of phase-boundary slip

The energy absorption of the DPLs generally depends on the plateau stress level and densification strain; it can be optimized if each phase is fully deformed by keeping a constant volume fraction of reinforcement grains in each column k/n. From the above analysis, notable distinctions appear among the C-*fcc* and other types of DPLs regarding their mechanical properties and deformation modes, which we can attribute to the interactions among reinforcement grains and different deformation behavior around phase boundaries. In addition to truss yielding and plastic deformation observed in dispersive DPLs with the interacted reinforcement grains, trusses around phase boundaries deformed more severely in compact DPLs; this led to enhanced plastic deformation, truss fracture and frictional energy that occurred with the interacted reinforcement grains sliding along the phase boundaries (Fig. 2B). It is apparent that such phase-boundary slip provides an additional contribution to the increased energy dissipation in the compaction type DPLs. The area S of the phase-boundary slip area can be determined in terms of the contacting area between the blocks of matrix phase and reinforcement phase in the compression direction, as illustrated in Fig. 7A; this is also examined by simulation to identify any effects on mechanical performance. DPLs with four different phase-boundary slip areas S were designed, as indicated by the yellow lines in Fig. 7B, all with a constant volume $\overline{V}_{RP}$ of reinforcement phase. In the first model, $S = 0$ represents no through-thickness connections between the reinforcement grains and matrix phase lattice materials. We assume the slip area of the second model as a baseline with $S = S_0$, then for the third model of C-*fcc* DPLs, we have $S = 2S_0$; in addition, an optimized DPL with $S = 4S_0$ was included in the analysis. All the four models were simulated with the resulting predicted stress-strain curves compared in Fig. 7C, where it is clear that the compressive stiffness, strength and energy absorption all increase with the slip area S.

Accordingly, an optimized DPLs with the maximum slip area, where every lattice unit in the matrix phase is completely surrounded by reinforcement phase lattice, can be designed with coherent phase boundaries, as shown in Fig. 7D; this is termed Opt-*fcc*. The corresponding specific energy absorption from our simulation is compared to that of other types of dual-phase mechanical metamaterials in Fig. 3C, where it can be seen that the SEA of the Opt-*fcc* material is as high as 24.3 J/g, which is ~2.5 times higher that of the constituent matrix phase lattice materials, ~67% higher than that of C-*fcc*, and even more than 33% higher than that of the Co-*fcc*. This demonstrates that stiff and tough dual-phase mechanical metamaterials can be designed with optimal energy absorption capability for applications requiring impact protection.

4. Summary and conclusions

In summary, novel dual-phase mechanical lattice metamaterial composites have been proposed from the perspective of enhancing strength and toughness through bioinspired phase manipulation and patterning. Architected lattice materials with different topological microstructures were employed, respectively, as (soft) matrix and (hard) reinforcement phases. The resulting dual-phase composite lattice (DPL) materials were printed with austenitic stainless-steel powders and mechanically tested. Based on our experimental results and simulations, the following conclusions can be made:

1) Deformation and failure in the dual-phase lattice materials initiate in the matrix phase which subsequently triggers shear localization bands that bypass the reinforcement grains.
2) Experimental values reveal that, after the addition of the reinforcement grains, the stiffness, strength and specific energy absorption of the DPLs all increase, respectively by ~50%, 49%, 45%, as compared to the corresponding properties of the constituent matrix phase.
3) By fully utilizing the energy dissipation associated with phase-boundary slip, DPLs with a maximum slip area between the reinforcement and matrix phases exhibit a maximum specific energy absorption capability which is up to ~2.5 times of that of their constituent SPLs.
4) The rationale for designing dual-phase metamaterials with excellent energy absorption capacity is summarized with a focus on phase patterning as:
   a) The mechanical properties of the reinforcement phase SPLs should be greater than those of matrix phase.
   b) The densification strain and stress of each phase, and the difference between the densification stress of two phases, should be as high as possible for greater energy absorption.
   c) The volume fraction of reinforcement phase should be the same in each column to make sure each lattice cell can be fully compressed.
   d) The reinforcement grains should be connected but not overlapping, satisfying $L = 2L_{\mathrm{RG}}$ with the greatest phase-boundary area, where every truss unit in the matrix phase is completely surrounded by reinforcement phase lattices.

The dual-phase mechanical composite metamaterials proposed in this study can emulate almost any of Nature's architectures and toughening mechanisms, forming strong and tough digital metamaterials/composites with programmable phase patterns. Despite their complex architectures, these metamaterials can be fabricated simply by any existing single-material printing approaches. Also, their performance can be manipulated easily by selecting each phase of any topology, geometry and function, which will largely expand material design space.

Authors contribution statement

W.H.G. and H.T.W. fabricated all the samples, W.H.G., Y. H. and H.T.W. carried out mechanical testing, W.H.G. and R.H.Y. performed metallographic and optical observation, W.H.G. and J. X. developed the theoretical model, W.H.G. D.H.C. and Z.H.H carried out simulation of the DPLs, all under the supervision of S.Y. and R.O.R. S.Y. and R.O.R. wrote the manuscript with assistance from all authors.

CRediT author statement

Sha Yin: Conceptualization, Validation. Supervision. Writing-Original draft preparation. Reviewing and Editing. Weihua Guo: Formal analysis. Huitian Wang: Experimental testing. Yao Huang: Experimental testing. Ruiheng Yang: Experimental testing. Zihan Hu: Formal analysis. Dianhao Chen: Formal analysis. Jun Xu: Formal analysis. Robert Ritchie: Validation. Supervision. Writing-Original draft preparation. Reviewing and Editing.

Declaration of Competing Interest

The authors declare no competing interests.

Acknowledgments

This work was supported by BUAA-CAIP United Laboratory supported by Changshu Automotive Trim Co., Ltd and the Fundamental Research Funds for the Central Universities, Beihang University. ROR acknowledges support from the H.T. & Jessie Chua Distinguished Professorship at Berkeley.

Appendix A. Theoretical stiffness

To predict the stiffness of the DPL, theoretical stiffness models for each constituting phase were first derived based on the previous literature (Yin et al., 2018) as shown in Fig. A1. For MP SPLs, the compressive stiffness has been expressed as:

$$E_{MP} = \frac{\sqrt{2}\pi d_2^2}{6 l_2^2} E_S \lambda_{N2} \lambda_{B2} \tag{A1}$$

where $\lambda_{N2}$and λ_{B2}represent the contributions from the respective effects of nodal volume and bending deformation. With the sc-*fcc* lattice as the reinforcement phase, the equivalent unit cell can be divided into three parts such their effects on compressive stiffness can be similarly deduced, as:

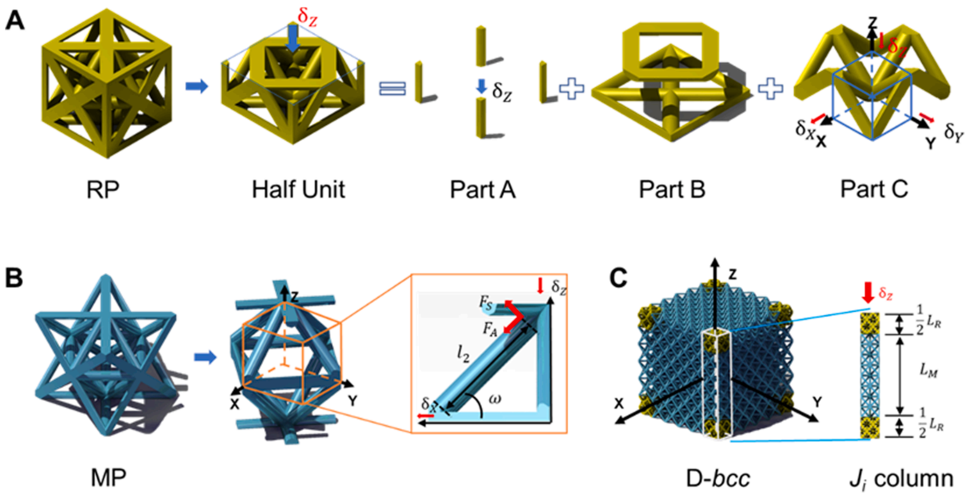

Fig. A1. Theoretical stiffness analysis for DPLs. (A) Illustration of *sc-fcc* type RP. (B) Loading conditions in the *z*-direction. (C) Selected column for analysis.

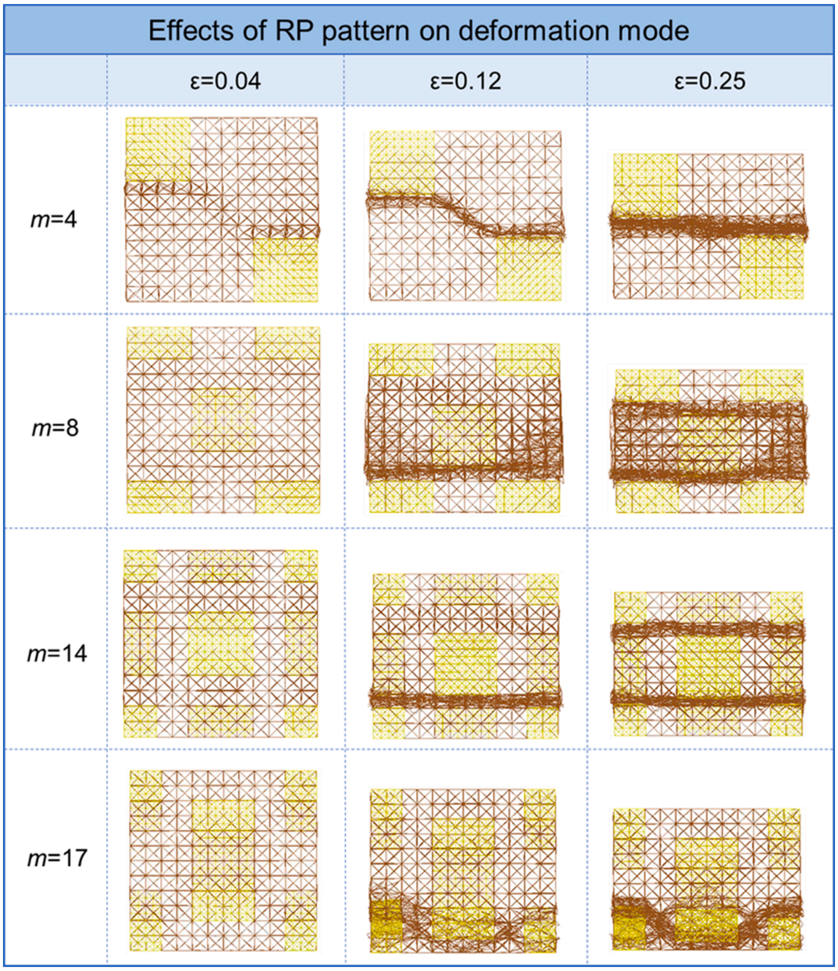

Fig. A2. Various shear band patterns due to different dispersions of RGs.

$$E_{MP} = \frac{\pi d_1^2}{4 l_1^2} E_S \lambda_{N1} \lambda_{B1} \tag{A2}$$

where $\lambda_{N1} = \lambda_{B1} = 1$, representing no contribution from nodal volume and bending deformation effects of the lattice trusses. The predicted values agree well the experimental results, as shown in Table 2.

The stiffness of the DPL was theoretically deduced by calculating the contribution from each column and neglecting the interactions between them. For the imposed displacement δ_Z in the z-direction shown in Fig. A1, the strain in a column can be calculated by considering a random column J_i for analysis and assuming that the compressive stress in the matrix phase equals that in the reinforcement. This strain should then be $\varepsilon_i = \varepsilon_{M_i} + \varepsilon_{R_i}$, with $\varepsilon_{M_i} = \delta_{M_i}/L_{M_i}$ and $\varepsilon_{R_i} = \delta_{R_i}/L_{R_i}$; here, ε_{M_i} and δ_{R_i} are, respectively, the deformation of the matrix and reinforcement phases in the column J_i, with $L_{M_i} = n - k$ and $L_{R_i} = k_i$ representing the length of these phases. Note that n is the overall cell number, and k_1 is the cell number of the reinforcement grains in column J_i. This leads to:

$$\frac{E_{RP}}{E_{MP}} = \frac{k_i \delta_{M_i}}{(n - k_i)\delta_{R_i}} \tag{A3}$$

where the stiffness of this column E_{J_i} is given by:

$$E_{J_i} = \frac{n E_{RP} E_{MP}}{(n - k_i) E_{RP} + k_i E_{MP}} \tag{A4}$$

Accordingly, for the dual-phase materials, the stiffness E can be expressed as:

$$E = \sum_{i-1}^{n^2} E_{J_i} \tag{A5}$$

Appendix B. Energy absorption

Energy absorption per unit volume was calculated as the area under the stress-strain curve up to the densification strain ε_D , given as:

$$EA = \int_0^{\varepsilon_D} \sigma d\varepsilon. \tag{B1}$$

For an arbitrary column J_i, according to the idealized compressive curves as illustrated in the Fig. 2C, we can have:

$$(EA)_{\mathrm{J_i}} = (EA)_{\mathrm{J_i}}^{\mathrm{I}} + (EA)_{\mathrm{J_i}}^{\mathrm{II}} \tag{B2}$$

$$(EA)_{\mathrm{J_i}}^{\mathrm{I}} = \sigma_D^{MP}\left(\varepsilon_{2_i} - \frac{1}{2}\varepsilon_{1_i}\right) \tag{B3}$$

$$(EA)_{\mathrm{J_i}}^{\mathrm{II}} = \frac{1}{2}\left(\sigma_D^{MP} + \sigma_D^{RP}\right)\left(\varepsilon_{D_i} - \varepsilon_{2_i}\right) \tag{B4}$$

where

$(EA)_{\mathrm{J_i}}$ - energy absorption per unit volume of column J_i;

$(EA)_{\mathrm{J_i}}^{\mathrm{I}}$ - energy absorption per unit volume from the matrix phase dominated stage I;

$(EA)_{\mathrm{J_i}}^{\mathrm{II}}$- energy absorption per unit volume from the reinforcement phase dominated stage II;

ε_1- yield strain of the DPLs;

ε_2- densification strain of the matrix phase in the DPLs;

σ_D^{MP}- densification stress of the matrix phase SPLs;

σ_D^{RP}- densification stress of the reinforcement phase SPLs.

With the iso-stress assumption, this gives:

$$\varepsilon_{1_i} = \frac{n - k_i}{n} \frac{\sigma_D^{MP}}{E_{MP}} + \frac{k_i}{n} \frac{\sigma_D^{MP}}{E_{RP}} \tag{B5}$$

$$\varepsilon_{2_i} = \frac{n - k_i}{n} \varepsilon_D^{MP} + \frac{k_i}{n} \frac{\sigma_D^{MP}}{E_{RP}} \tag{B6}$$

where

ε_D^{MP}- densification strain of the matrix phase SPLs;

ε_D^{RP}- densification strain of the reinforcement phase SPLs;

E_{MP}- the stiffness of the matrix phase SPLs;
E_{RP}- the stiffness of the reinforcement phase SPLs.

Thus:

$$(EA)_{J_i}^{I} = \sigma_D^{MP}\left(\frac{n-k_i}{n}\varepsilon_D^{MP} - \frac{1}{2}\frac{n-k_i}{n}\frac{\sigma_D^{MP}}{E_{MP}} + \frac{1}{2}\frac{k_i}{n}\frac{\sigma_D^{MP}}{E_{RP}}\right) \tag{B7}$$

$$(EA)_{J_i}^{II} = \frac{1}{2}\left(\sigma_D^{MP} + \sigma_D^{RP}\right)\left(\frac{n-k_i}{n}\Delta\varepsilon_i + \frac{k_i}{n}\varepsilon_D^{RP} - \frac{k_i}{n}\frac{\sigma_D^{MP}}{E_{RP}}\right) \tag{B8}$$

Accordingly, the overall energy absorption of column J_i is given as:

$$(EA)_{J_i} = \frac{n-k_i}{n}(EA)_{MP} + \frac{1}{2}\frac{k_i}{n}\left(\sigma_D^{MP} + \sigma_D^{RP}\right)\varepsilon_D^{RP} + \frac{1}{2}\frac{n-k_i}{n}\left[\frac{\left(\sigma_D^{RP}\right)^2 - \left(\sigma_D^{MP}\right)^2}{\psi}\right] - \frac{1}{2}\frac{k_i}{n}\frac{\sigma_D^{MP}\sigma_D^{RP}}{E_{RP}} \tag{B9}$$

where $(EA)_{MP} = \sigma_{MP}\left(\varepsilon_D^{MP} - \frac{1}{2}\frac{\sigma_{MP}}{E_{MP}}\right)$ is the energy absorption of the matrix phase SPLs. The energy absorption of the DPLs is therefore:

$$(EA) = \frac{1}{n^2}\sum_{i=1}^{n^2}(EA)_{J_i} \tag{B10}$$

References

Aizenberg, J.C.W., Thanawala, M.S., Sundar, V.C., Morse, D.E., Fratzl, P., 2005. Skeleton of euplectella sp.: Structural hierarchy from the nanoscale to the macroscale. Science 309 (5732), 275–278.
Berger, J.B., Wadley, H.N., McMeeking, R.M., 2017. Mechanical metamaterials at the theoretical limit of isotropic elastic stiffness. Nature 543, 533–537.
Deng, S., Wu, J., Dickey, M.D., Zhao, Q., Xie, T., 2019. Rapid open-air digital light 3D printing of thermoplastic polymer. Adv. Mater., e1903970
Deshpande, V.S., Fleck, N.A., Ashby, M.F., 2001a. Effective properties of the octet-truss lattice material. J. Mech. Phys. Solids 49 (8), 1747–1769.
Deshpande, V.S., Ashby, M.F., Fleck, N.A., 2001b. Foam topology bending versus stretching dominated architectures. Acta Mater. 49 (6), 1035–1040.
Evans, A.G., He, M.Y., Deshpande, V.S., Hutchinson, J.W., Jacobsen, A.J., Carter, W.B., 2010. Concepts for enhanced energy absorption using hollow micro-lattices. Int. J. Impact Eng. 37, 947–959.
Evans, A.G., Hutchinson, J.W., Fleck, N.A., Ashby, M.F., Wadley, H.N.G., 2001. The topological design of multifunctional cellular metals. Prog. Mater. Sci. 46, 309–327.
Gazizov, M., Kaibyshev, R., 2017. Precipitation structure and strengthening mechanisms in an Al-Cu-Mg-Ag alloy. Mat. Sci. Eng. A. 702, 29–40.
Gu, G.X., Takaffoli, M., Buehler, M.J., 2017. Hierarchically enhanced impact resistance of bioinspired composites. Adv. Mater. 29, 1700060.
Haghpanah, B., Salari-Sharif, L., Pourrajab, P., Hopkins, J., Valdevit, L., 2016. Multistable shape-reconfigurable architected materials. Adv. Mater. 28, 7915–7920.
Han, S.C., Lee, J.W., Kang, K., 2015. A new type of low density material: Shellular. Adv. Mater. 27, 5506–5511.
Jin, S., Ngai, T., Zhang, G., Zhai, T., Jia, S., Li, L., 2018. Precipitation strengthening mechanisms during natural ageing and subsequent artificial aging in an Al-Mg-Si-Cu alloy. Mat. Sci. Eng. A. 724, 53–59.
Lee, J.H., Wang, L., Boyce, M.C., Thomas, E.L., 2012. Periodic bicontinuous composites for high specific energy absorption. Nano Lett. 12, 4392–4396.
Liu, Y., Wang, L., 2015. Enhanced stiffness, strength and energy absorption for co-continuous composites with liquid filler. Compos. Struct. 128, 274–283.
Meza, L.R., Das, S., Greer, J.R., 2014. Strong, lightweight, and recoverable three-dimensional ceramic nanolattices. Science 345 (6202), 1322–1326.
Meza, L.R., Greer, J.R., 2014. Mechanical characterization of hollow ceramic nanolattices. J. Mater. Sci. 49, 2496–2508.
Meza, L.R., Zelhofer, A.J., Clarke, N., Mateos, A.J., Kochmann, D.M., Greer, J.R., 2015. Resilient 3D hierarchical architected metamaterials. Proc. Natl. Acad. Sci. USA 112, 11502–11507.
Mohr, D., 2017. Large deformation response of additively-manufactured FCC metamaterials: f rom octet truss lattices towards continuous shell mesostructures. Int. J. Plasticity 92, 122–147.
Mohr, D., 2018. Elastically-isotropic truss lattice materials of reduced plastic anisotropy. Int. J. Solids Struct. 138, 24–39.
Munch, E., Launey, M.E., Alsem, D.H., Saiz, E., Tomsia, A.P., Ritchie, R.O., 2008. Tough, bio-inspired hybrid materials. Science 322, 1516–1520.
Pham, M.S., Liu, C., Todd, I., Lertthanasarn, J., 2019. Damage-tolerant architected materials inspired by crystal microstructure. Nature 565, 305–311.
Pingle, S.M., Fleck, N.A., Deshpande, V.S., Wadley, H.N.G., 2010. Collapse mechanism maps for a hollow pyramidal lattice. Proc. Roy. Soc. A. 467, 985–1011.
Ruschel, A.L., Zok, F.W., 2020. A bi-material concept for periodic dissipative lattices. J. Mech. Phys. Solids 145, 104144.
Shan, S., Kang, S.H., Raney, J.R., Wang, P., Fang, L., Candido, F., Lewis, J.A., Bertoldi, K., 2015. Multistable architected materials for trapping elastic strain energy. Adv. Mater. 27, 4296–4301.
Tancogne-Dejean, T., Diamantopoulou, M., Gorji, M.B., Bonatti, C., Mohr, D., 2018. 3D plate-lattices: An emerging class of low-density metamaterial exhibiting optimal isotropic stiffness. Adv. Mater. 30, e1803334.
Thielen, M., Schmitt, C.N., Eckert, S., Speck, T., Seidel, R., 2013. Structure-function relationship of the foam-like pomelo peel (Citrus maxima) - An inspiration for the development of biomimetic damping materials with high energy dissipation. Bioinspir. Biomim. 8, 025001.
Velasco-Hogan, A., Xu, J., Meyers, M.A., 2018. Additive manufacturing as a method to design and optimize bioinspired structures. Adv. Mater. 30, e1800940.
Wadley, H.N., 2006. Multifunctional periodic cellular metals. Philos. Trans. A. 364, 31–68.
Wang, B., Wu, L., Ma, L., Sun, Y., Du, S., 2010. Mechanical behavior of the sandwich structures with carbon fiber-reinforced pyramidal lattice truss core. Mater. Des. 31, 2659–2663.
Wang, L., Lau, J., Thomas, E.L., Boyce, M.C., 2011. Co-continuous composite materials for stiffness, strength, and energy dissipation. Adv. Mater. 23, 1524–1529.

Weaver, J.C., Milliron, G.W., Miserez, A., Evans-Lutterodt, K., Herrera, S., Gallana, I., Mershon, W.J., Swanson, B., Zavattieri, P., DiMasi, E., Kisailus, D., 2012. The stomatopod dactyl club: a formidable damage-tolerant biological hammer. Science 336 (6086), 1275–1280.
Wu, G., Chan, K.C., Zhu, L., Sun, L., Lu, J., 2017. Dual-phase nanostructuring as a route to high-strength magnesium alloys. Nature 545, 80–83.
Wu, Q., Vaziri, A., Asl, M.E., Ghosh, R., Gao, Y., Wei, X., Ma, L., Xiong, J., Wu, L., 2019. Lattice materials with pyramidal hierarchy: systematic analysis and three dimensional failure mechanism maps. J. Mech. Phys. Solids 125, 112–144.
Yashpal, Y., Sumankant, S., Jawalkar, C.S., Verma, A.S., Suri, N.M., 2017. Fabrication of aluminium metal matrix composites with particulate reinforcement: a review. Mater. Today 4, 2927–2936.
Yin, S., Chen, H., Yang, R., He, Q., Chen, D., Ye, L., Mai, Y-W., Xu, J., Ritchie, R.O., 2020. Tough nature-inspired helicoidal composites with printing-induced voids. Cell Rep. Phys. Sci. 1.
Yin, S., Jacobsen, A.J., Wu, L., Nutt, S.R., 2013. Inertial stabilization of flexible polymer micro-lattice materials. J. Mater. Sci. 48, 6558–6566.
Yin, S., Li, J., Chen, H., Ritchie, R.O., Xu, J., 2018. Design and strengthening mechanisms in hierarchical architected materials processed using additive manufacturing. Int. J. Mech. Sci. 149, 150–163.
Zhang, W., Yin, S., Yu, T.X., Xu, J., 2019a. Crushing resistance and energy absorption of pomelo peel inspired hierarchical honeycomb. Int. J. Impact Eng. 125, 163–172.
Zhang, Y., Li, B., Zheng, Q.S., Genin, G.M., Chen, C.Q., 2019b. Programmable and robust static topological solitons in mechanical metamaterials. Nat. Commun. 10, 5605.
Zheng, X., Smith, W., Jackson, J., Moran, B., Cui, H., Chen, D., Ye, J., Fang, N., Rodriguez, N., Weisgraber, T., Spadaccini, C.M., 2016. Multiscale metallic metamaterials. Nat. Mater. 15, 1100–1106.